Effects of radiative cooling on advection fog over the Northwest Pacific Ocean: Observations and large eddy simulations

Liu Yang[1], Saisai Ding[2], Jing-Wu Liu[2*], Su-Ping Zhang[2]

[1]College of Aviation Meteorology, Civil Aviation Flight University of China, Guanghan, China

[2] Frontier Science Center for Deep Ocean Multispheres and Earth System (FDOMES), Physical Oceanography Laboratory, and Ocean–Atmosphere Interaction and Climate Laboratory, Ocean University of China, Qingdao, China

* Corresponding author: Jing-Wu Liu, Ocean University of China, 238 Songling Road, Qingdao, 266100, P. R. China

Email: liujingwu@126.com; liujingwu@ouc.edu.cn

Abstract

During boreal summer, prevailing southerlies traverse the sharp sea surface temperature (SST) front in the Northwest Pacific (NWP) Ocean, creating a stable air-sea interface characterized by surface air temperature (SAT) higher than SST, which promotes the frequent occurrence of advection fog. However, long-term shipborne observations reveal that during episodes of advection fog, SAT usually decreases below SST, with a peak relative frequency (~34.5%) to all fog obervations before sunrise and a minimum relative frequency (~18.8%) before sunset. From a Lagrangian perspective, this study employs a turbulence-closure large-eddy simulation (LES) model to trace a fog column across the SST front and investigates how SAT drops below SST during an advection fog event. The LES model, incorporating constant solar radiation, successfully simulates the evolution of advection fog and the negative difference between SAT and SST. Simulation results show that once the near-surface air condenses, thermal turbulence is generated by strong longwave radiation cooling (LWC) at the fog top. The influence of LWC on the fog layer surpasses the cooling effect of the near-surface mechanical turbulence ~2 hours after the fog formation, while the fog column is still positioned over the SST front. When the fog column arrives at the cold flank of the SST front, the top-down developing mixed layer induced by the LWC reaches the surface, causing SAT to drop below SST. The LES model with diurnal solar radiation successfully simulates the observational diurnal variation in SAT-SST during the fog event, suggesting that the model captures the essential processes responsible for negative SAT-SST. This study highlights the significance of fog-top cooling and its associated thermal turbulence in the evolution of advection fog. Given the challenges faced by numerical weather prediction models in forecasting sea fog, our findings suggest that observations of negative SAT-SST during advection fog episodes present an opportunity to enhance the performance of these models in simulating the thermal turbulence induced by the LWC at the fog top.

1. Introduction

The northwest Pacific Ocean experiences heavy sea fog during summer (Wang, 1985; Koračin and Dorman, 2017), which is of great importance due to its significant impact on maritime activities (Gultepe et al., 2007; Trémant, 1987). However, present numerical weather prediction models struggle to accurately forecast sea fog (Gao et al., 2007), partly because their coarse resolutions inadequately resolve boundary-layer processes within the thin fog layer with depths of hundreds of meters (Yang et al., 2019). Therefore, enhancing our understanding of turbulent boundary-layer processes becomes imperative for refining the accuracy of sea fog predictions.

The sea surface temperature (SST) gradient associated with Kuroshio Extension often triggers advection fog during summertime warm advection (Wang, 1985; Koračin and Dorman, 2017). Prevailing southerlies on the western flank of the subtropical high transport warm, humid air across Kuroshio Extension front (Zhang et al., 2014; Long et al., 2016; Koracin and Dorman, 2017), which cools the near-surface humid air through mechanical turbulence, leading to air saturation and fog formation (Taylor, 1917; Rodhe, 1962; Lewis et al., 2004; Gao et al., 2007; Yang et al., 2020). Nevertheless, near-surface cooling induced by mechanical turbulence appears to be crucial in the initial phase of advection fog (Hu et al., 2006).

Once fog forms, longwave radiation cooling (LWC) effect at the fog top commences to influence fog evolution. Earlier observational studies conjectured that the LWC at the fog top plays an important role in the fog's development and maintenance (Douglas, 1930; Lamb, 1943; Petterssen, 1938; Findlater et al., 1989). LWC at the fog top induces negative buoyancy and thermal turbulence (Bretherton and Wyant, 1997; Gerber et al., 2005, 2013; Guan et al., 1997; Yamaguchi and Randall, 2008; Koračin and Dorman, 2017). This thermal turbulence further promotes vertical mixing and cools the fog layer (Rogers and Koračin, 1992; Koracin et al., 2001, 2005; Yang et al., 2018). Huang et al. (2015) identified a so-called thermal turbulence interface, which separates thermal turbulence induced by the fog-top LWC and near-surface mechanical turbulence. Despite previous studies recognizing the significance

67   of LWC at the fog top, its relative importance to near-surface cooling by mechanical

68   turbulence remains to be determined.

69   Observational evidence underscores the significance of LWC at fog top, as surface

70   air temperature (SAT) occasionally falls below SST during advection fog episodes. This

71   means that the sea surface acts to heat the fog layer (referred to as sea fog with sea

72   surface heating [ssH] hereafter). Instances of ssH fog have been reported in advection

73   fog events over the Yellow Sea (Zhang et al., 2012; Zhang and Ren, 2010), during the

74   haar peak over the North Sea (Lamb et al., 1943), and in the fog off the California coast

75   (Leipper, 1948, 1994), as well as off the northeastern coast of Scotland (Findlater et al.

76   1989). Based on long-term buoy observations, Yang et al. (2018) found that the relative

77   frequency of ssH fog to advection fog reaches up to ~30% over the Yellow Sea in

78   summer. Their composite analysis revealed that ssH fog is associated with stronger

79   atmospheric subsidence, a drier free atmosphere, and sharper capping inversions,

80   indicative of a crucial role of the fog-top LWC for ssH fog. However, limited

81   observations of the boundary-layer vertical structure over the sea inhibit the

82   understanding of how fog-top LWC influences advection fog and leads to a negative

83   SAT-SST.

84   In comparison to numerical weather prediction models, large eddy simulations

85   (LES) with higher resolutions are capable of explicitly resolving larger thermal

86   turbulent eddies within the boundary layer. LES has been successfully employed in

87   studies related to clouds (Bretherton and Wyant, 1997; Wyant et al., 1997; Stevens 2000,

88   2007; Savic-Jovci and Stevens, 2008; McGibbon and Bretherton, 2017) and continental

89   fog (Nakanishi, 2000; Bergot, 2013, 2016; Mazoyer et al. 2016; Maronga and Bosveld

90   2017; Schwenkel and Maronga 2019). Recently, the application of LES has extended

91   to sea fog (Yang et al., 2021; Wainwright and Richter, 2021). Yang et al. (2021) used

92   the climatological subsidence to force a LES model to study an advection fog event

93   over the NWP. They found that the fog-top thermal turbulence induced by the LWC

94   entrains the drier free atmospheric air into the boundary layer, which evaporates near-

95   surface fog droplets, leading to a transition of fog into stratus. This simulated fog-to-

96   stratus transition based on LES is consistent with that in long-term observations.

97   Wainwright and Richter (2021) attempted to use LES to examine the sensitivity of sea

98   fog to the cloud-droplet number concentration, turbulent mixing, and SAT-SST.

99   The present study primarily focuses on the ssH fog during advection fog episodes.

100   We first analyze the statistical features of the ssH fog over the NWP using long-term

101   shipborne observations. ssH fog was observed during the advection fog episode studied

102   by Yang et al. (2021). Thus, this study extends the LES simulation conducted by Yang

103   et al. (2021) by forcing the LES with more realistic free-atmospheric subsidence to

104   specifically investigate the boundary-layer processes responsible for ssH fog. We

105   quantify the heat budgets of the fog layer based on the LES results to compare the

106   effects of fog-top LWC and near-surface cooling and identify the interface between

107   thermal and mechanical turbulence. The results highlight the importance of the fog-top

108   cooling and its induced thermal turbulence on the evolution of advection fog.

109   The paper is organized as follows. Section 2 describes the data sets and methods

110   used in this study. Section 3 analyzes the observational characteristics of sea fog with

111   ssH over the NWP. Section 4 presents the simulation results obtained using constant

112   solar radiation and diurnal cycle radiation. Section 5 provides a summary and

113   discussions.

114

2. Data and method

2.1 ICOADS and ERA5

117   We employ shipborne observations provided by the International Comprehensive

118   Ocean–Atmosphere Data Set (ICOADS) to investigate the occurrence of sea fog over

119   the summer NWP. Fog is identified when the present-weather code is between 10 and

120   12 or between 40 and 49, and the visibility is lower than 1 km (Bari et al., 2016; Yang

121   et al., 2021). Additionally, we also use SST, SAT, and 10 m winds to examine the sea-

122   air interface conditions during sea fog. We include $\sim 6 \times 10^4$ fog reports over the NWP

123   between 1998 and 2018 to explore sea fog climatologies and select a fog case that took

124   place during 1- 4 July 2013 for further analysis and simulation.

125   To construct the idealized initial conditions for the sea fog simulation, we use the

126 fifth generation of the European Centre for Medium-Range Weather Forecasts

127 atmospheric reanalysis (ERA5, Hersbach et al., 2020). ERA5 fields are on a 0.25° ×

128 0.25° grid with 16 levels below 500 hPa.

129 **2.2 UCLA-LES model**

130 UCLA-LES is a three-dimensional, turbulence-closure boundary layer model with

131 prognostic variables such as total water mixing ratio q_t, liquid water potential

132 temperature θ_l, ang three components of wind. This model is often used to simulate

133 stable, neutral, and convective boundary layers (Stevens et al., 2005).

134 The parameterization for subgrid fluxes in UCLA-LES is based on the

135 Smagorinsky–Lilly model (Smagorinsky, 1963; Lilly, 1967) to satisfy the model

136 closure. This model can explicitly compute thermal turbulent flux and appropriately

137 describe turbulent mixing process within the boundary layer (Stevens et al., 2005; Jiang

138 et al., 2006). Surface fluxes of momentum, temperature, and moisture are computed

139 based on similarity theory (Stevens et al., 2010). We set specific surface properties to

140 represent oceanic conditions and prescribe surface temperature and specific humidity.

141 Radiative transfer calculations are performed using the δ-four-stream method (Fu and

142 Liou, 1993; Pincus and Stevens, 2009), and radiative fluxes are based on background

143 profiles of pressure, temperature, humidity, and ozone content (Stevens et al., 2003).

144 The model has a warm-rain microphysical scheme (Seifert and Beheng, 2001) assuming

145 that cloud droplets are in equilibrium at a fixed concentration. The microphysics

146 process accounts for the interactions within the same type and between different types

147 of cloud an raindrops. We set a specified 100×10^6 g kg^{-1} cloud-droplet mixing ratio in

148 our simulations. To capture the delicate radiative and turbulent processes, we set

149 horizontal grid spacing as 20 m and the vertical grid spacing as 1 m below 50 m and 5

150 m above 50 m. The simulation domain is 1500 m × 1500 m × 2000 m.

151 **2.3 Diagnostic equations**

152 We analyze the budget of domain-averaged heat and water vapor to investigate the

153 related physical processes responsible for sea fog evolution. The heat budget is

154 calculated using

$$155 \qquad \frac{\partial \bar{\theta}}{\partial t} = -\frac{\partial \overline{w'\theta'}}{\partial z} - \frac{L_v E}{\bar{\rho} C_p} - \frac{1}{\bar{\rho} C_p} \frac{\partial \bar{Q}}{\partial z}, \qquad (1)$$

156 where θ is potential temperature. The term on the right-hand side (RHS) describes the

157 heat change from turbulent mixing, latent heat releasing, and the radiation effect,

158 respectively. $\overline{w'\theta'}$ is the sum of resolved and sub-scale parameterized turbulent heat

159 flux. E is the amount of water vapor produced by liquid phase transition. L_v is the latent

160 heat release of condensation or evaporation. ρ is air density. $C_p = 1004.67$ J kg^{-1} K^{-1} is

161 specific heat of moist air. Q is radiation flux. The water vapor budget equation is

$$162 \qquad \frac{\partial \bar{q_v}}{\partial t} = -\frac{\partial \overline{w'q_v'}}{\partial z} + \frac{E}{\bar{\rho}}, \qquad (2)$$

163 where q_v is water vapor mixing ratio. The terms on the RHS describe the q_v change from

164 turbulent mixing effect and evaporation/condensation. $\overline{w'q_v'}$ is the sum of resolved and

165 sub-scale turbulent water vapor flux.

166   To diagnose the turbulent mixing process responsible for heat and moisture variation,

167 we compute the turbulent kinetic energy (TKE) budget using

$$168 \qquad \frac{\partial \overline{TKE}}{\partial t} = +\frac{g}{\bar{\theta_v}} \left(\overline{u_3'\theta_v'} \right) - \overline{u_i'u_3'} \frac{\partial \overline{u_i}}{\partial x_3} - \frac{\partial \left(\overline{u_3'TKE} \right)}{\partial x_3} - \varepsilon, \qquad (5)$$

169 where subscripts $i = 1$, 2, and 3 represent x, y, and z coordinates. The four terms on the

170 RHS represent buoyancy production, mechanical production from wind shear, the

171 vertical transport of TKE, and TKE dissipation due to friction, respectively.

172

3. Advection fog with ssH in ICOADS observations

3.1 Statistical features of ssH fog

175   To isolate advection fog, we trace back each ICOADS fog observation for 48 hours

176 by integrating ERA5 winds at 10 m. We define the fog observations from warmer waters

177 as advection fog in this study and obtain 43,105 advection fog observations during the

178 period of 1998-2018. Figure 1 shows the climatological frequency of advection fog,

179 advection fog with sea surface cooling (ssC, when SAT-SST > 0), and advection fog

180 with ssH over the NWP during June-July-August (JJA). Advection fog is frequently

181 observed on the cold flank of the Kuroshio Extension front, with a peak frequency of

182 ~30% near the Kuril Islands, where intense tidal mixing results in SSTs below 10°C

183   (Fig. 1a; Tokinaga and Xie, 2009). Advection fog with ssC primarily appears in a band-

184   shaped region between 40°N and 52°N, a distribution similar to that of all advection

185   fog (Figs. 1a and b). The frequency of ssH fog also peaks at ~10% near the Kuril Islands

186   (Fig. 1c), but its region of maximal occurrence extends further downstream to the north

187   of 52°N. A detailed comparison of Figs. 1a and 1b suggests that approximately half of

188   the ssC fog transitions into ssH fog as the fog column migrates northward under

189   prevailing southwesterlies.
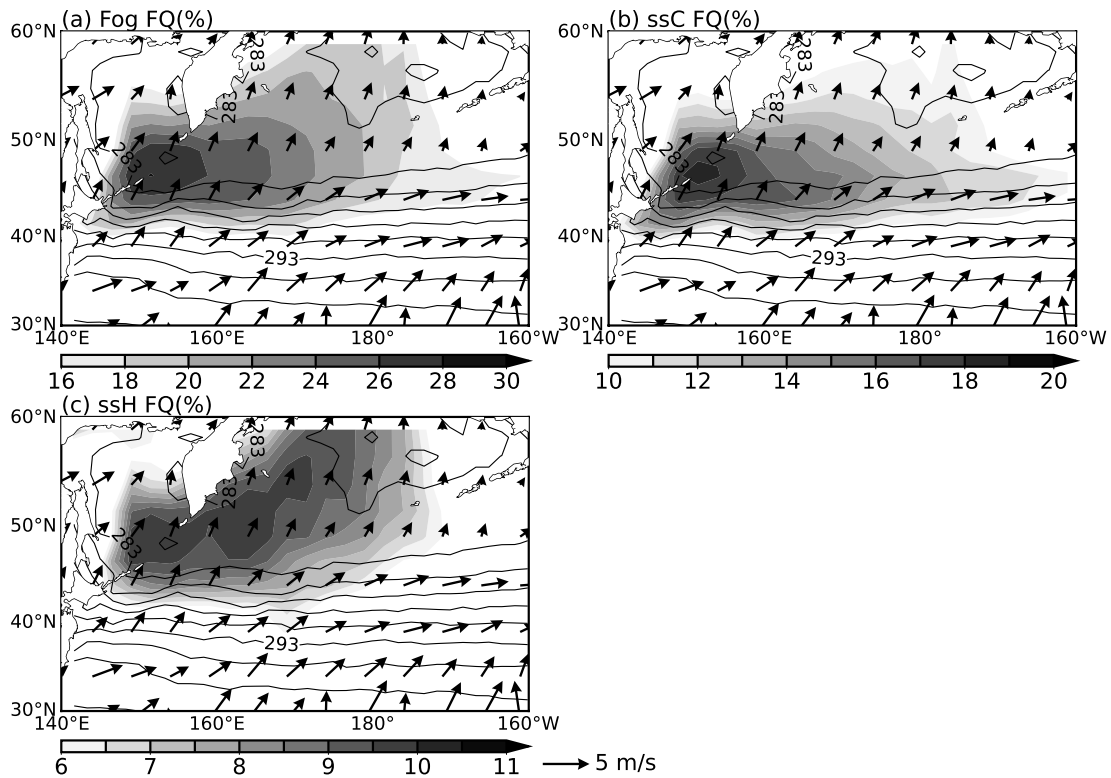
190

191   FIG. 1 Climatological SST (contours with 2-K intervals), surface winds (vectors, m s⁻¹), and frequencies

192   (shading, %) of (a) advection fog, advection fog with (b) ssC and (c) ssH during June-July-August for

193   1998-2018. The SST and winds are based on ERA5, and the fog frequencies are obtained from ICOADS.

194   Figure 2 illustrates the probability density function (PDF) of simultaneous SAT-

195   SST values concurrent with advection fog over the NWP during JJA. The majority of

196   these SAT-SST values are positive (Fig. 2), consistent with the observational results of

197   Fu and Song (2014). However, a substantial proportion (~27.5%) of advection fog in

198   the NWP is associated with ssH fog. Based on coastal buoy observations, Yang et al.

199   (2019) reported that ~30% of SAT falls below SST during fog events in the Yellow Sea.

200   Li et al. (2022) also observed ~32% fog is with ssH over the northeast Pacific during

201   winter. The consistent observations of advection fog with ssH imply that cooling

202 mechanisms other than near-surface turbulent cooling have a substantial impact on the

203 evolution of advection fog.
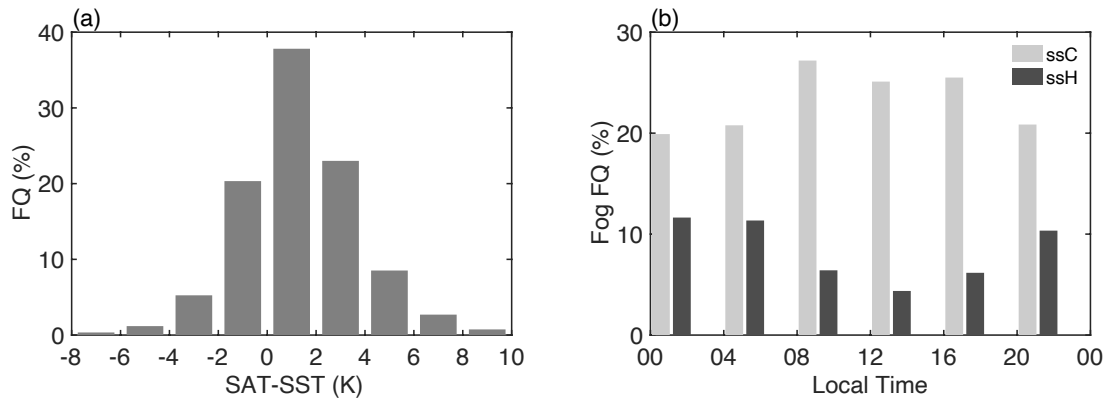
204

205 FIG. 2 (a) Probability density function (%) of SAT-SST (°C) concurrent with advection fog
206 observations over the NWP (30-60°N, 140-200°E) during June-July-August based on ICOADS. (b)
207 The frequencies of advection fog with ssH (dark grey bars) and ssC (light grey) as functions of local
208 time.

209   There is a noticeable diurnal variation in ssH fog over the NWP (dark grey bars in

210 Fig. 2b). Local time is determined based on the universal time of fog observations and

211 their respective longitudes. The frequency of ssH fog reaches its maximum (~11.5%)

212 and minimum (~4%) during 0000-0400 and 1200-1600 local time, respectively (the

213 dark grey bars in Fig. 2b). Relative to all advection fog occurrences, the frequency of

214 ssH fog is ~18.8% during the daytime and increases to ~34.5% at night. In contrast, the

215 frequency of ssC fog is highest around sunrise (the light grey bars in Fig. 2b) and does

216 not exhibit a clear diurnal variation. The evident diurnal cycle of ssH fog over the open

217 sea is new to our knowledge and suggests that the radiative balance over fog top

218 significantly alters the evolution of advection fog.

219 **3.2 An ssH fog case**

220   We examine an advection fog event during 01- 04 July 2013 over the NWP.

221 Satellite images observed by the Moderate Resolution Imaging Spectroradiometer

222 (MODIS) captured clear fog patches at 1000 local standard time (LST) 01-03 July near

223 the Kuril Islands and over the northwest Pacific (Fig. 3b). The synoptic steady

224 southwesterlies over the SST front caused the fog event (Fig. 4), and ICOADS

225 observations reported no precipitation during this period. Further information regarding

226 this fog event can be found in Yang et al. (2021). Our primary focus is on the negative

227 SAT-SST observations during this fog episode (Fig. 4). Fog was first reported near the

228 Kuril Islands at the night of 30 June (red stars in Figs. 2b), concurring with positive

229 SAT-SST. The southwesterly winds, along with positive SAT-SST, signify the event as

230 advection fog. As the saturated air moved northeastward (Figs. 3b-d and 4e-h), negative

231 SAT-SST was detected within the fog patch during 02-04 July (blue stars in Figs. 4e-h).

232 Notably, most of the ssH fog occurred at night. Figure 5 shows the time series of

233 observational SAT-SST closest to the trajectory in Fig. 4. After fog formation, there is

234 a noticeable diurnal variation in the sea-air temperature difference, with air temperature

235 dropping below SST during the nights of 02 and 03 July. The minimum sea-air

236 temperature difference reaches -1 K at 2200 LST on 03 July.
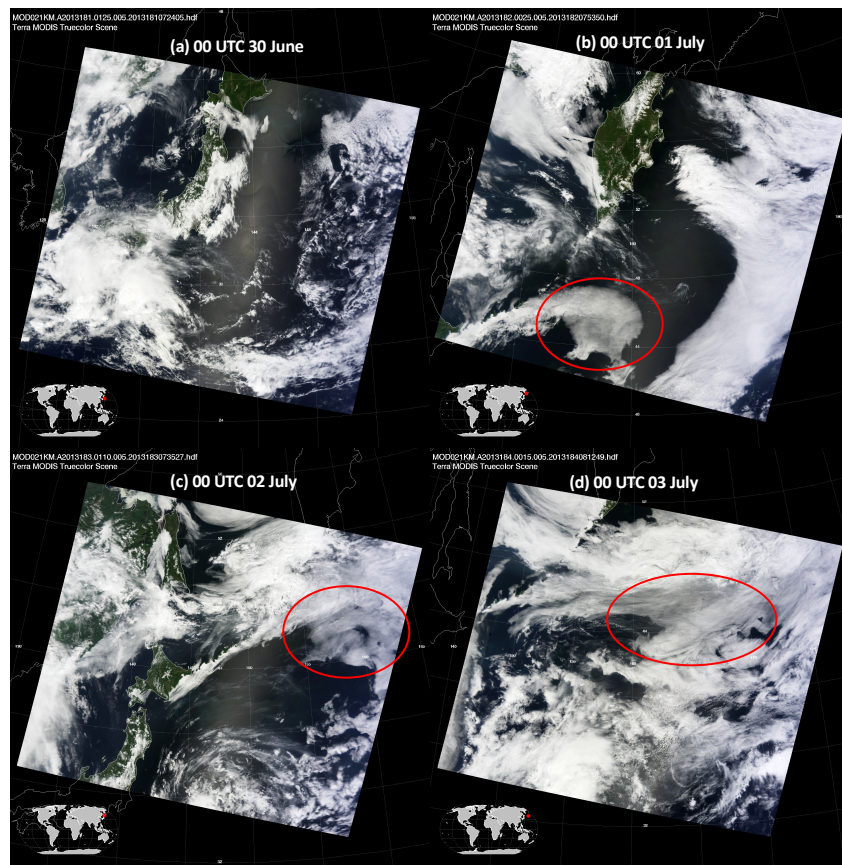
237

238 FIG. 3 Visible satellite images from MODIS.
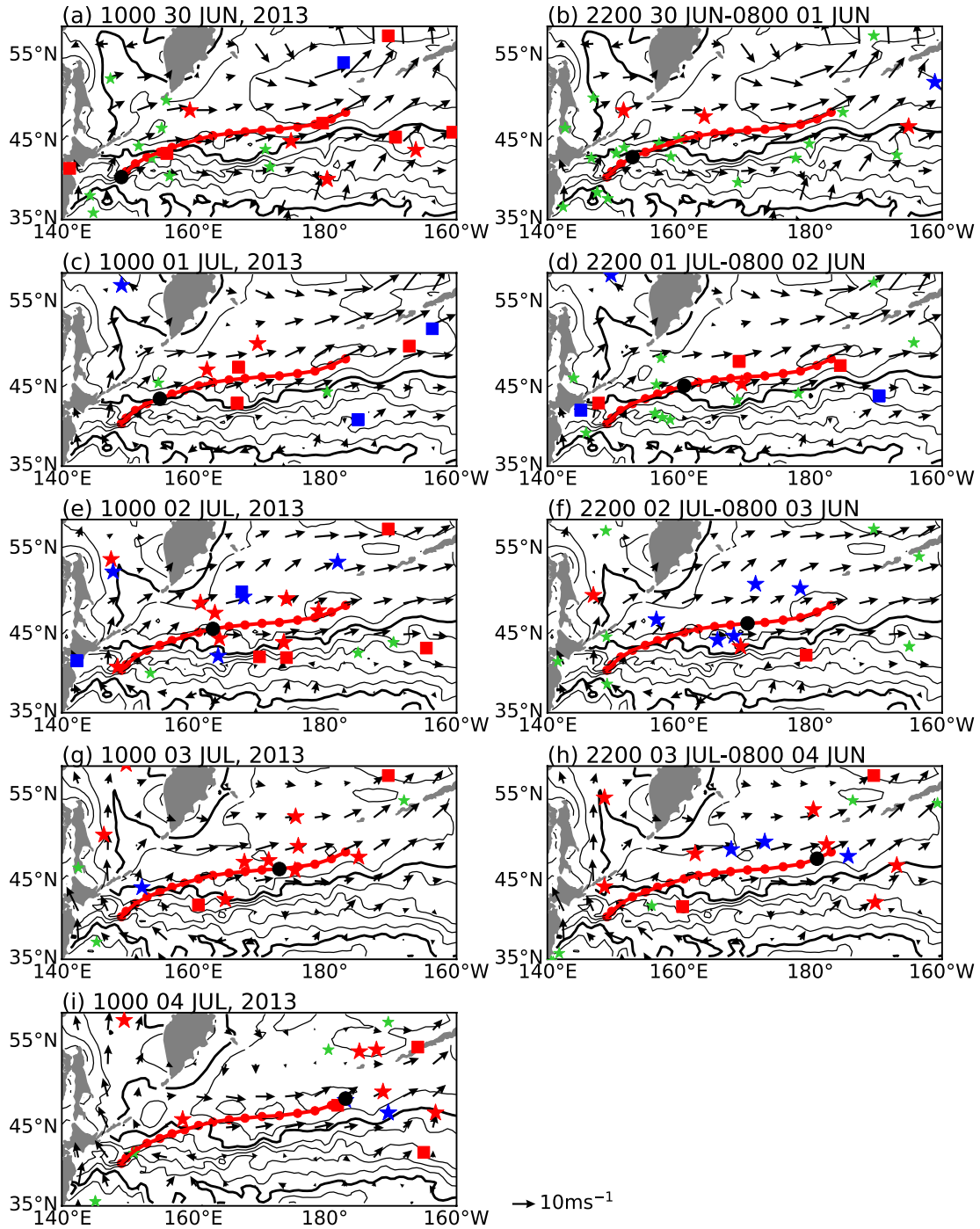
FIG. 4 ICOADS observations of the advection fog event during 30 June - 04 July, 2013. The blue and red stars represent ssH and ssC fog, respectively, and squares indicate stratus, and green stars indicate other cloud types or clear sky. The ICOADS observations and ERA5 10-m winds near 1000 LST from 30 June to 04 July are shown in (a), (c), (e), (g), and (i), respectively. The ICOADS reports and ERA5 winds between 2200-0800 (+1 day) LST are shown in (b), (d), (f), (h), respectively, to include more nighttime observations. The thick red line in each panel demonstrates the 4-day back trajectory from the ssH fog observation at 49.6°N 183.2°E, and the red dots are the location of the trajectory every 6 hours, and larger black dot indicating the location at the corresponding time of the panel. The contours are averaged ERA5 SST during 30 June-04 July, and the thick contours indicate 283, 293 and 303 K, respectively.
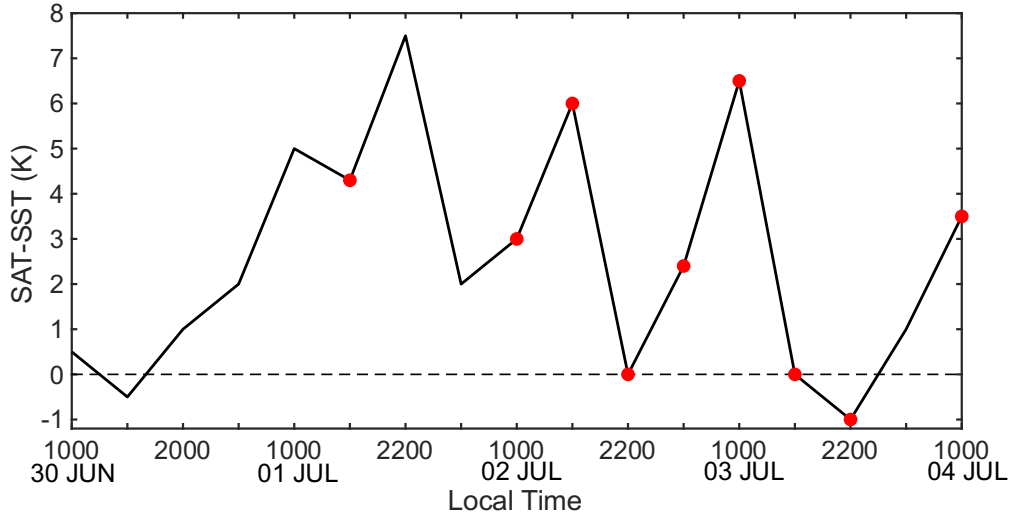
250

251 FIG. 5 ICOADS observations of SAT-SST closed to the trajectory in Fig. 4. The red dots indicate fog

252 occurrences.

4 Simulation with constant solar radiation

4.1 Simulation setups

255   The synoptic processes associated with the fog event detailed in subsection 3b

256 align closely with the climatological characteristics of ssH and ssC fog (Figs. 1 and 2).

257 To uncover the boundary-layer processes responsible for the ssH fog, we use the

258 UCLA-LES model to simulate this typical fog event from a Lagrangian perspective.

259 We trace back an ssH fog observation at 49.6 °N 183.2 °E in Fig. 4i, which had an SAT-

260 SST value of -1.2 °C. This trajectory is roughly consistent with the one obtained using

261 HYSPLIT trajectory model (Draxler and Rolph, 2010; not shown). The air column

262 consecutively experienced no fog, ssC, and ssH fog along the trajectory from 30 June

263 to 04 July, 2013 (Figs. 4 and 5).

264   We prescribe time-varying SST and large-scale divergence to force the boundary

265 layer evolution. To fit the observations, we simplify the observational SST by

266 employing a cosine function during the initial 36 h, succeeded by a constant value of

267 8 °C (not shown). The fog case and the simulation setups are the same as those in Yang

268 et al. (2021), except for the divergence forcing in the free-atmosphere. We apply a

269 realistic divergence of 2×10^{-6} s^{-1}, which is the averaged value along the trajectory and

270 is double the climatological value in Yang et al. (2021). We first perform a simulation

271 with fixed solar radiation.

272   We generate idealized initial conditions for the simulation by integrating ERA5

273   and satellite data. Cloud–Aerosol Lidar and Infrared Pathfinder Satellite Observations

274   (CALIPSO) indicated a boundary layer height of 400 m (not shown). We establish a

275   typical clear-sky boundary layer structure by linearizing the original ERA5 profiles into

276   three parts: The mixed layer, inversion, and free troposphere. Within the 400 m deep

277   mixed layer, θ and q_t profiles remain constant (Figs. 7a and b). Above the mixed layer,

278   an inversion with a 6 K jump in θ is present (Fig. 7a). In the free troposphere, θ and q_t

279   decrease at the rate of -6.6 K km^{-1} (Fig. 7a) and -4 g kg^{-1} km^{-1} (Fig. 7b), respectively.

280   Throughout the simulation, winds of 9.6 m s^{-1} in geostrophic balance are applied.

281   **4.2 Evolution in boundary-layer structure**

282   Figure 6a depicts the time-height section of liquid water mixing ratio (q_l) and

283   virtual potential temperature (θ_v) for the air column in the simulation with constant solar

284   radiation. We exclude the first 2 hours of results due to the model's spin-up. Liquid

285   water initially appears near surface (~20 m) at 0400 local standard time (LST) 01 July

286   and rapidly extends to the surface within 1 h, resulting in fog formation. We define fog

287   when q_l exceeds 0.02 g kg^{-1} (Kunkel, 1984). Fog persists until 0200 LST on 4 July,

288   transitioning into stratus as the near-surface droplets evaporate. This transition results

289   from the entrainment of the free-atmospheric dry air caused by the fog-top LWC (Yang

290   et al., 2021). The height of the fog top grows from 20 to 380 m until 0000 LST 03 July

291   and rarely varies thereafter. CALIPSO passed through the fog area and observed cloud-

292   top heights of about 300 m and 400 m on 0000 LST 02 July and 0100 LST 03 July (not

293   shown), respectively, which is very close to simulated results. The capping inversion

294   intensifies from 5 to 12 K after fog formation due to the fog layer cooling (Fig. 5a).
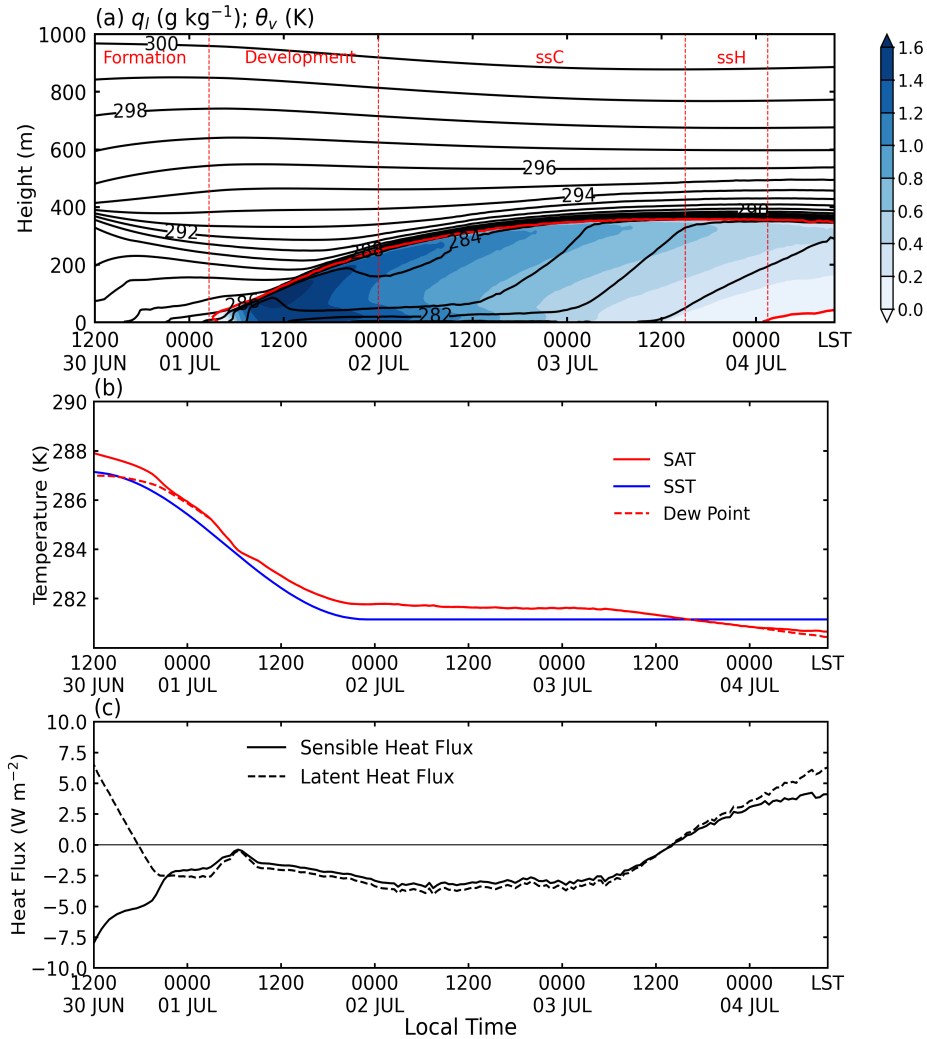
FIG. 6. (a) Time-height section of simulated liquid water mixing ratio (shading, g kg^{-1}), virtual potential temperature (contours, K) for constant solar radiation simulation. Red lines indicate the fog/cloud top and bottom, respectively. (b) SAT (red line, K), SST (blue, K) and surface dewpoint temperature (dashed red, K). (c) Same as (b) but for surface sensible heat flux (solid, W m^{-2}) and latent heat flux (dashed, W m^{-2}). Upward sensible and latent heat fluxes are positive. Red dashed lines in (a) divide the evolution process of fog into the four phases described in the article.

The model successfully reproduces the ssH fog. Over the SST front, SAT follows the underlying SST with a difference of 0.8 K, resulting in strong downward sensible heat flux between -7.5 and 0 W m^{-2} (Figs. 6b and 6c). At 0400 LST on 01 July, SAT drops to the dewpoint at 285.8 K. After crossing the SST front, SAT is almost constant during the period of 0000 LST on 02-03 July but quickly decreases afterward, falling below SST at 1700 LST on 03 July (Fig. 6b). The occurrence time of ssH fog is consistent with ICOADS observations. The minimum air-sea temperature difference during sea fog is -0.65 K, weaker than the observed -1 K (Figs. 5 and 6b). From this

310   time, both sensible and latent heat fluxes change their directions, indicating that the

311   ocean begins to heat and moisten the surface air (Figs. 5b and 5c). The ssH fog sustains

312   for 12 hours.

313   We divide the simulation into four phases: fog formation (from 1200 LST on 30

314   June to 0400 LST on 01 July) and development (from 0400 LST on 01 July to 0000

315   LST on 02 July) over the SST front, followed by fog maintenance with ssC (from 0000

316   LST on 02 July to 1700 LST on 03 July) and ssH (from 1700 LST on 03 July to 0200

317   LST on 04 July) to the north of the SST front. Figure 6 shows boundary layer structure

318   for the above four phases. The soundings of θ_v, total water mixing ratio (q_t), and q_l are

319   domain-averaged at the selected times.
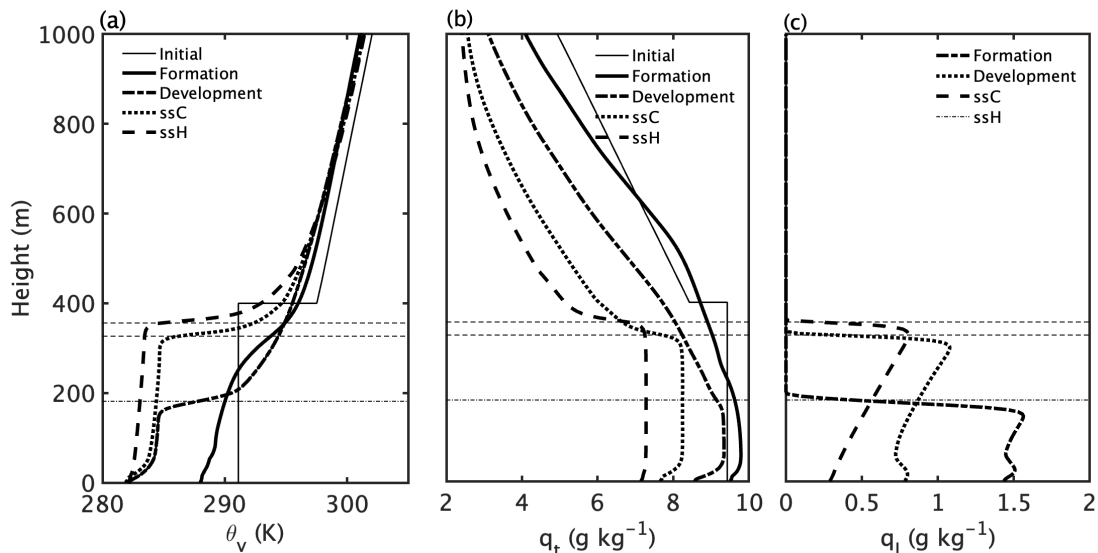
320

321   FIG. 7. Horizontal mean soundings for constant solar radiation simulation at 1000 LST on 30 June (thin
322   solid line), 2000 LST on 30 June (solid), 1200 on LST 01 July (dot-dashed), 1200 LST on 02 July (dot)
323   and 2000 LST on 03 July (dashed). (a) Virtual potential temperature (K), (b) total water mixing ratio (g
324   kg^{-1}) and (c) liquid water mixing ratio (g kg^{-1}). Horizontal dot-dahsed line represents fog top height at
325   1200 on 01 July, and the horizontal dashed line represents fog top heights at 1200 on 02 July and 2000
326   on 03 July.

327   Before fog formation, the cold sea surface efficiently cools the near-surface air,

328   creating a stable boundary layer (Figs. 6a and 7a). q_t increases with height below 20 m

329   and remains nearly constant within the boundary layer (Fig. 7b). The upward decrease

330   in air temperature and increase in q_t result in the maximal relative humidity and

331   saturation occurring near 20 m (Fig. 7a). Once fog forms, a mixed layer develops

332   downward from the fog top to 50 m, capping the original stable layer produced by the

cold sea surface (Fig. 7a). θ_v and q_t of the boundary layer decrease by ~6 K and ~1 g

kg^{-1}, respectively, from 2000 LST on 30 June to 1200 LST on 01 July (Figs. 7a and 7b).

Large q_l near fog top converses into rainwater and descends, resulting in a secondary

peak of q_l near the surface at about 20 m (Fig. 7c). The stratifications of θ_v, q_t and q_l

indicate a different cooling mechanism at the fog top from that at its bottom (Fig. 7a).

During the ssC fog phase, a well-mixed boundary layer develops, and θ_v decreases

by 1 K from 1200 LST on 01 July to 1200 LST on 02 July (Figs. 7a and 7b). q_l peaks

near the fog top (Fig. 7c). During the ssH fog phase, the sea surface heats and moistens

the fog layer (Fig. 6b), while the fog layer keeps cooling and drying at a much slower

rate (Fig. 7a), indicating that the LWC effect at the fog top dominates the fog cooling

and maintenance. The thermal and moisture stratifications of ssH fog share a similar

structure to those of ssC fog but with a deeper well-mixed layer (the long dashed lines

in Fig. 7).

4.3 Heat and moisture budgets

Figure 8 shows the profiles of heat and water vapor budget terms at different

phases. Figures 9a and 9b show the time series of surface heat and water vapor budget

terms, respectively. Over the SST front, the turbulent mixing and longwave radiation

effects cool the air both near the surface and throughout the entire boundary layer (Figs.

8a and 9a). Fog forms due to the cooling of the air near the surface (Fig. 8a).
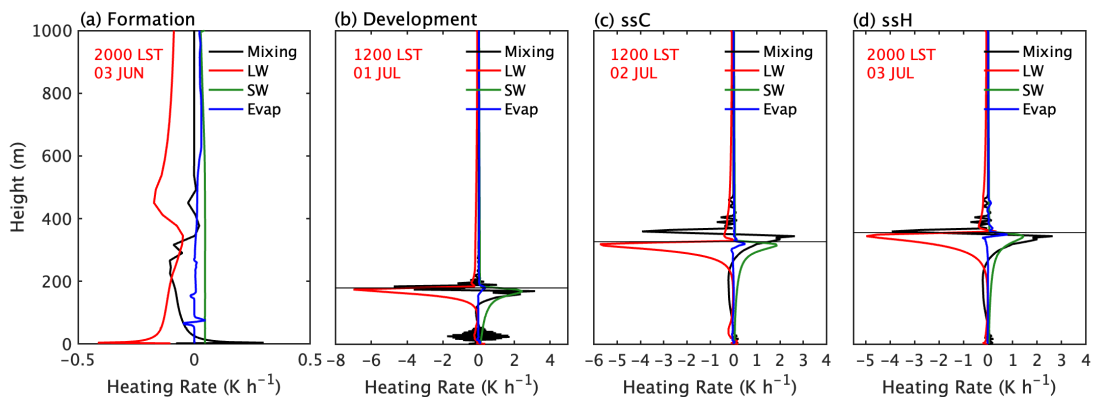
FIG. 8 Profiles of horizontal mean budget terms for heat (K h^{-1}) at (a) 2000 LST on 30, (b) 1200 LST on 01 July, (c) 1200 on 02 July and (d) 2000 LST on 03 July in the constant solar radiation simulation. The horizontal lines indicate fog tops.

After fog formation, the surface turbulent cooling intensifies dramatically, peaking

at -1.35 K h^{-1}, leading to a marked decrease in SAT (Fig. 9a). The rapid growth of q_l

358   releases latent heat through condensation, which partly offsets the cooling effect from

359   turbulent mixing. Caldwell and Bretherton (2005) suggested that sedimentation has a

360   drying and heating effect on the surface layer. The impact of sedimentation for the heat

361   budget is relatively small compared to turbulent mixing and LWC, both at the surface

362   and within the boundary layer (not shown). Within the boundary layer, longwave

363   radiation effect induces strong cooling at the fog top, and the resultant turbulent mixing

364   cools the upper boundary layer (the red line in Fig. 8b). Additionally, thermal turbulence

365   helps entrain the warm, dry air from the free atmosphere, warming the air at the fog top

366   while cooling the air above the fog layer (the black line in Fig. 8b).

367   When the fog volume moves north of the SST front (0000 LST on 02 July onward),

368   the surface cooling effects become weak due to the fixed SST and turbulent mixing

369   keeps drying the surface air (Fig. 9). Strong LWC persists at the fog top, inducing

370   turbulent mixing that cools the entire fog layer (Figs. 7a and 8c). In this case, the effect

371   of the fog-top LWC overcomes the surface cooling effect, causing SAT to drop below

372   SST. During the ssH phase, the LWC at the fog top slightly weakens and the turbulent

373   mixing cooling dominates within the fog layer, causing SAT to continuously decrease

374   (Figs. 6b and 8d).
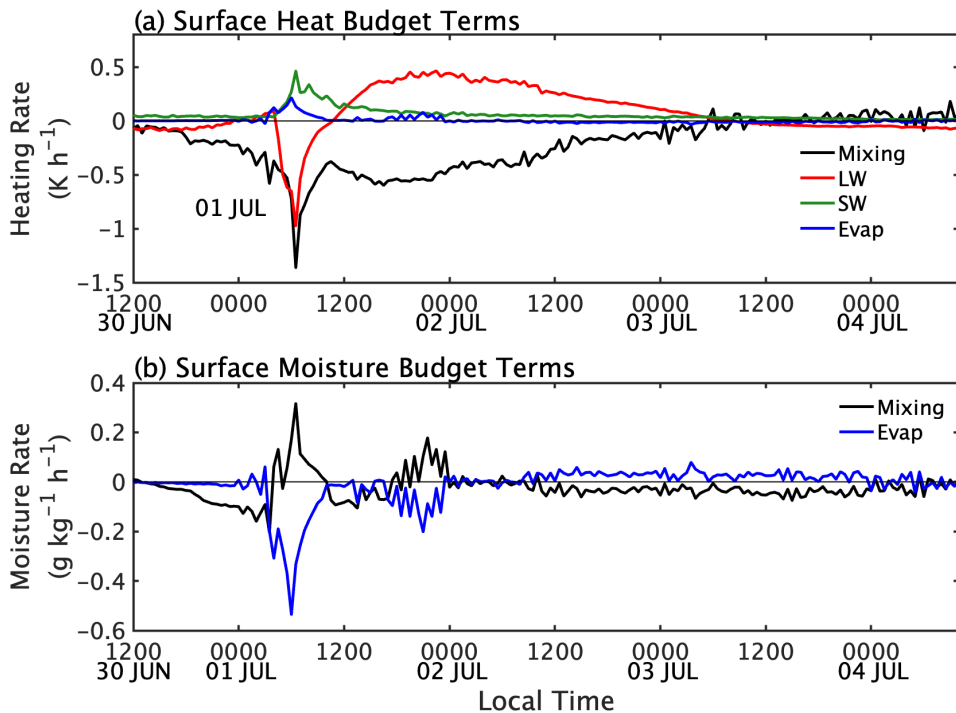
375

376   FIG. 9 Time series of horizontal mean budget terms at the surface for the constant solar radiation

377   simulation: (a) heat (K h^{-1}) and (b) water vapor (g kg^{-1} h^{-1}).

378   We quantify the heat budget for the fog layer by integrating heat budget for the fog

379   layer (Fig. 10). We determine the turbulent mixing term by calculating the difference

380   between the turbulent heat fluxes at the surface ($\overline{w'\theta'}_{sfc}$) and fog top ($\overline{w'\theta'}_{zi}$), z_i is fog

381   top height), representing the surface sensible heat transport and the effect of the fog-top

382   entrainment, respectively (the black and grey lines in Fig. 10). Prior to fog formation,

383   the surface sensible heat transport drives the boundary layer cooling (the black line in

384   Fig. 10). After the fog forms, the effect of longwave radiation acts to cool the boundary

385   layer due to the longwave heat loss at fog top (the red line). The LWC effect rapidly

386   exceeds surface cooling 2 hours after fog formation. Both shortwave radiation and

387   entrainment at the fog top warm the fog layer, partially offsetting the effects of surface

388   cooling and LWC.

389   The normalized LWC by the fog layer depth peaks 6 hours after fog formation and

390   then decreases rapidly (Fig. 10). This is possibly related to a negative feedback between

391   the fog-top radiative cooling and entrainment (Gerber et al. 2013, 2014). Following the

392   fog formation, an increase in fog-top entrainment causes a reduction in the liquid water

393   gradient at the fog top, which subsequently reduces the radiative cooling. This negative

394   feedback process takes several hours to take effect (not shown). Another reason for the

395   initial surge in LWC is the rapid growth of fog layer depth. In addition, we examine the

396   time-series maximum in LWC profiles (not shown), which fluctuates around 8 K h^{-1}

397   after fog formation and then steadily decreases. The fog-top LWC is somewhat less than

398   the counterpart for typical stratocumulus clouds (Curry and Herman 1985; Gerber et al.

399   2014). This may be attributed to the difference in free atmospheric humidity between

400   fog and stratocumulus scenes. In the case of stratocumulus clouds, the corresponding

401   descending motion results in drier air compared to the free atmosphere above fog. As

402   the fog moves to the cold flank of the SST front, the surface cooling weakens and

403   reverses, slightly heating the fog layer after SAT drops below SST. Overall, the

404   persistent and strong LWC at the fog top dominates the fog evolution, resulting in the

405   ssH fog.
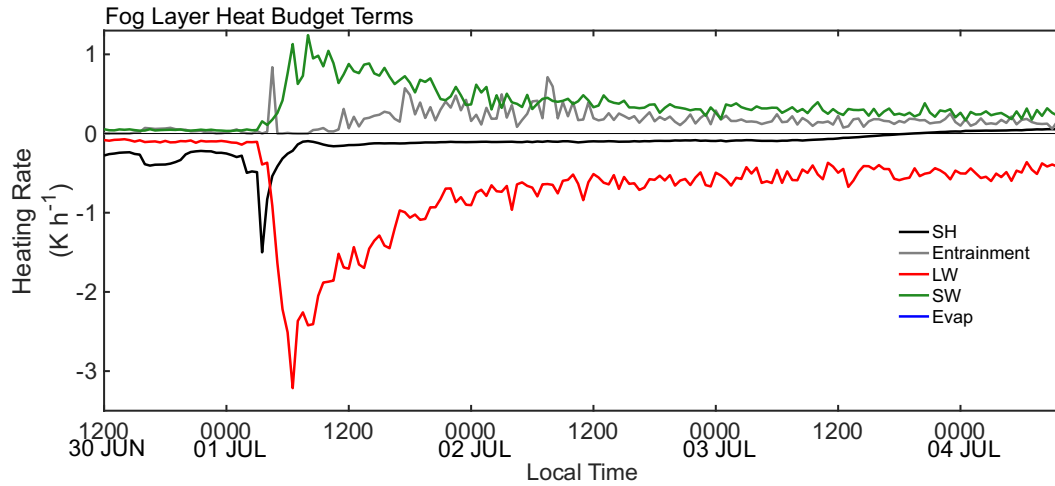
406

407 FIG. 10 Time series of horizontal mean heat budget terms (K h^{-1}) of the integral boundary layer for the

408 constant solar radiation simulation.

409 **4.4 TKE and its budget**

410 Figure 11 presents the time-height cross section of TKE for the simulation with

411 constant solar radiation. Prior to fog formation (0400 LST on 01 July), TKE exhibits a

412 relatively low magnitude below 200 m (Fig. 11), produced by the near-surface wind

413 shear and dissipated by friction and buoyancy (Fig. 12a). Mechanical turbulence

414 facilitates the transport of cooling from the surface, contributing to the fog formation.

415 Following fog formation, the LWC at the fog top induces buoyancy production of

416 turbulence over the upper boundary layer (Fig. 12b), leading to a noticeable peak in

417 TKE near the fog top ~12 hours after its formation (Fig. 11).
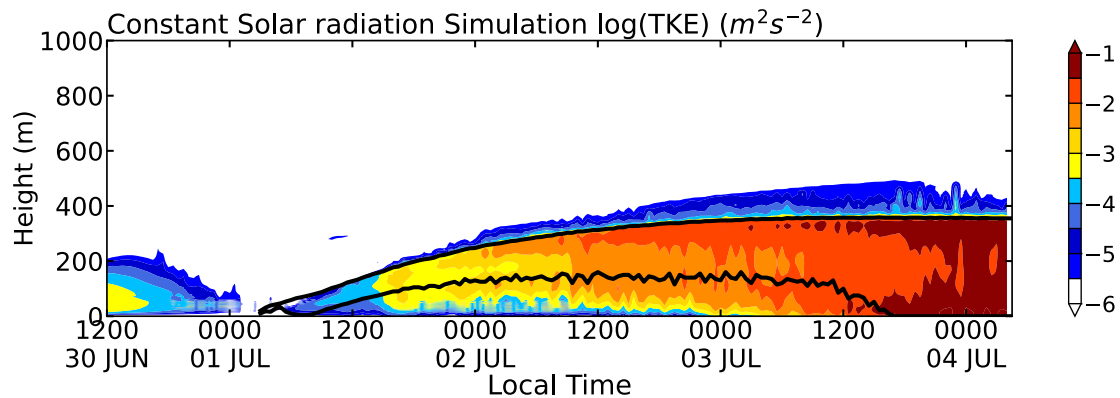
418

419 FIG. 11 Time-height section of log$_{10}$(TKE) (shading in m^2 s^{-2}), and time series of fog/cloud top height

420 (upper black lines in m) and thermal turbulence interface (lower black lines in m) for the simulations

421 with constant solar radiations.
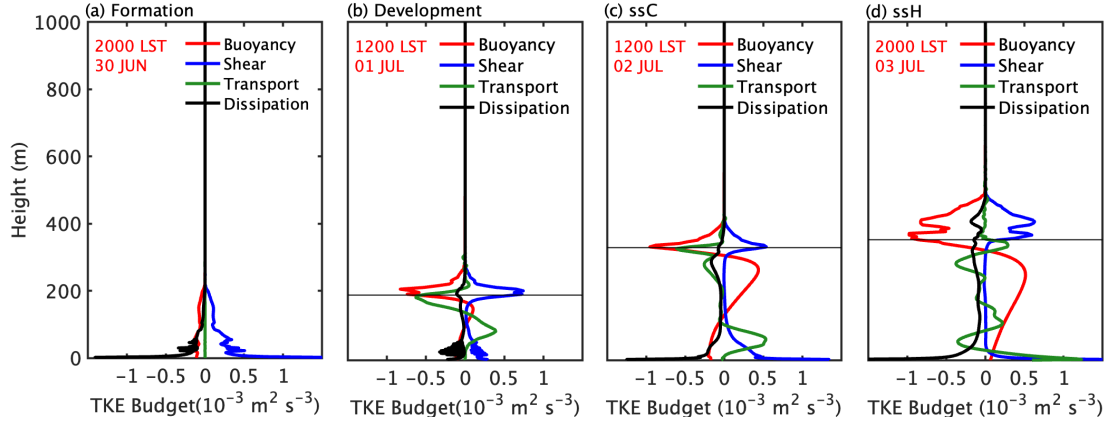
FIG. 12 Profiles of horizontal mean TKE budget terms (10^{-3} m^2 s^{-3}) for the constant solar radiation simulation at (a) 2000 LST on 30 June, (b) 1200 LST on 01 July, (c) 1200 LST on 02 July and (d) 2000 LST on 03 July. Thin black lines indicate fog tops.

Turbulence in the ssC fog intensifies after its formation at 0000 LST on 02 July (Fig. 11). The terms in TKE budget also exhibit a general strengthening trend from fog formation to the ssC fog (Fig. 12c). The generation of buoyancy-driven turbulence enhances and develops downward, leading to a deeper mixing layer within the boundary layer and cooling fog layer (Figs. 7a and 12c). TKE exhibits a significant increase from the ssC fog to ssH fog, particularly near the surface. This is because the air-sea interface becomes unstable (SAT-SST < 0), leading to the buoyancy production of turbulence (Fig. 12d). During this period, both buoyancy-induced and mechanically-induced turbulence contribute significantly to the maximum TKE near the surface.

The vertical structure of turbulence can be elucidated by employing the thermal turbulence interface, which distinguishes between the layers characterized by thermal and mechanical turbulence (Huang et al., 2015). Huang et al. (2005) defined a thermal turbulence interface as the gradient of the observational potential pseudo-equivalent temperature equals zero. Thermal turbulence induced by LWC is prevalent above the thermal turbulence interface, which is static unstable, whereas mechanical turbulence, aroused by wind shear, is predominant below the interface. Thermal turbulence interface helps to separate the fog layer into zones dominated by LWC and surface cooling. In this article, thermal turbulence interface is defined as the lowest altitude within the fog layer where the buoyancy production of turbulence is positive (the black lines in Fig. 11). Following fog formation, a thermal-turbulence mixing layer forms

446 beneath the fog top and extends across the upper half of the fog layer from 0000 LST

447 on 02 July (Fig. 11). After 0000 LST on 03 July, the mixing layer continues to develop

448 downward, eventually reaching the sea surface by 1500 LST on the same day, thus

449 establishing a well-mixed boundary layer. Subsequently, the thermal turbulence cools

450 the near-surface air and causes SAT to drop below SST after a 2-hour interval (Fig. 6b).

451 **5   Simulation with diurnal solar radiation**

452 We conduct an additional simulation that incorporates diurnal solar radiation.

453 Overall, the simulated fog with diurnal solar radiation exhibits similar behavior to that

454 in the simulation with constant solar radiation, but with clear diurnal variations. Fog

455 forms at 2200 LST on 30 June and rapidly grows. During the night, the stronger fog-

456 top LWC enhances thermal turbulence and entrainment, causing an increase in the fog

457 top height (Fig. 13a). In contrast, during the day, fog height decreased noticeably (Fig.

458 13a). With the continued drying effect of entrainment, liquid water content in the fog

459 layer decreases, ultimately causing the transition from fog to stratus at 1100 LST on 03

460 July (Fig. 13a).

461 The simulation incorporating diurnal solar radiation also generates ssH fog, which

462 exhibits significant diurnal variation. During the nights of 03 July and 04 July, SAT

463 rapidly drops below SST after sunset and recovers above SST after sunrise, which is

464 similar to the variations of observational SAT-SST (Figs. 5 and 13b). This result

465 indicates that the diurnal variation in the radiative balance over the fog top considerably

466 alters the transitions between ssC and ssH fog. The LWC at fog top has a clearer diurnal

467 variation and dominates the air-sea temperature differences (not shown). About 3-5

468 hours before sunset, the fog top LWC reach its minimum during a day. The

469 enhancement of LWC occurs approximately 3 hours earlier than the decline in air-sea

470 temperature difference, ultimately causing the air temperature falls below SST in the

471 early hours of 03 July (not shown). Additionally, both TKE and thermal-turbulence

472 mixing layer exhibit distinct diurnal variations (Fig. 14). The pronounced radiative

473 cooling at the fog top results in increased TKE and a thicker thermal-turbulence mixing

474 layer at nighttime compared to daytime (Fig. 14). The time period when the mixing

475 layer base and the ground coincide is the same as the occurrence period of ssH fog,

476 further demonstrating the regulating effect of LWC on the fog layer cooling.

477   We also conducted a simulation with intensified solar irradiance through an

478 increase in solar elevation angle to check the effect of solar irradiance. Sea fog

479 dissipates 8 hours earlier than that in the standard solar radiation experiment and

480 observations (not shown). Two hours before sea fog dissipation, there is the ssH fog

481 occurrence. Nevertheless, there are minimal changes in the evolution of the fog top

482 height and the thermal and dynamic structure of the boundary layer during sea fog.
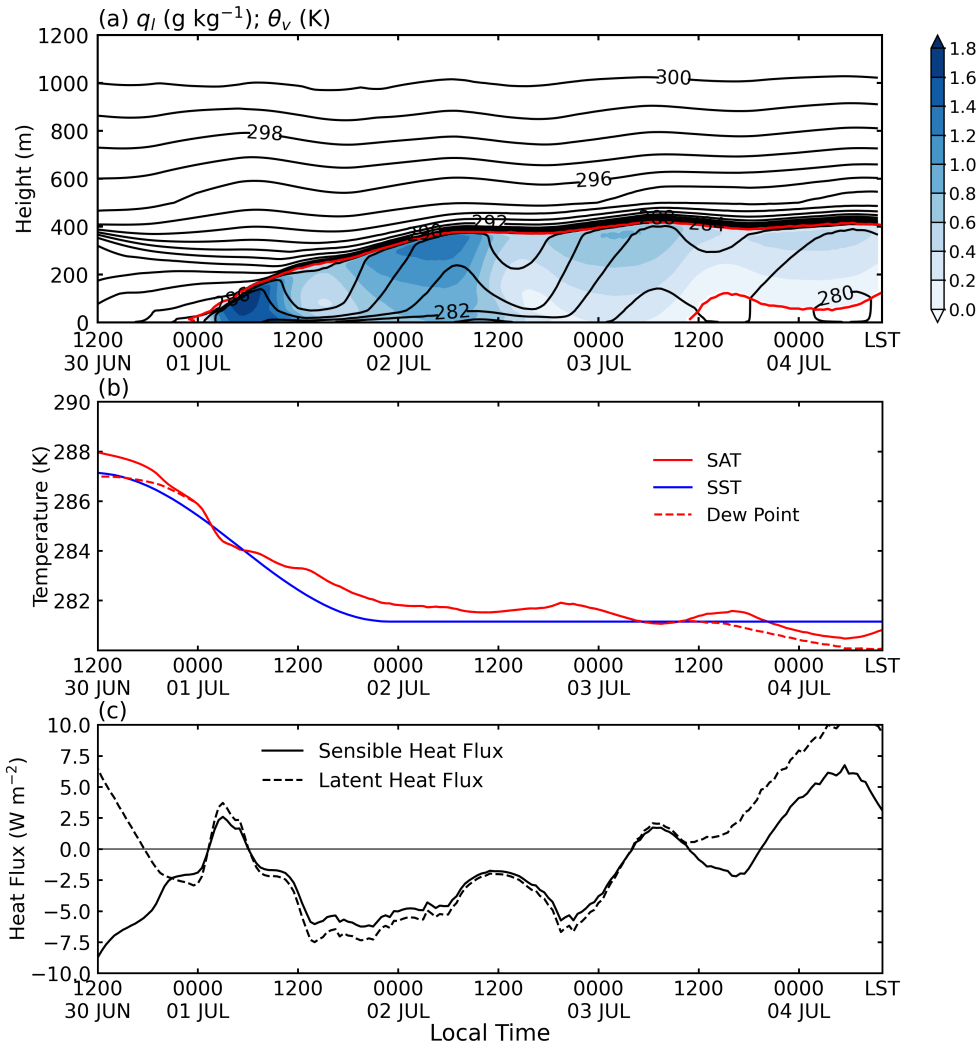
483

484 FIG. 13 As in Fig. 6, but for the simulation with diurnal cycle radiation.
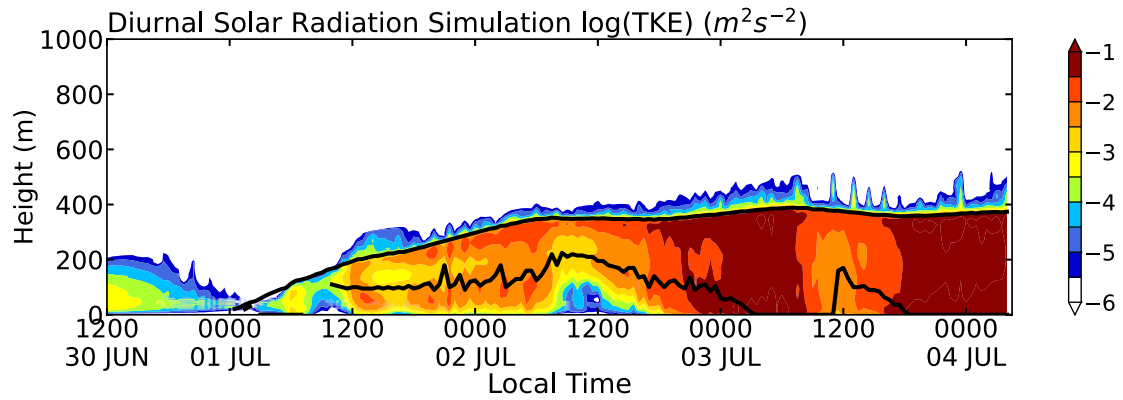
485

486   FIG. 14 As in Fig. 11, but for the simulation with diurnal cycle radiation.

6 Summary and discussion

488   Sea fog is of great importance due to its significant impact on maritime activities.

489   The present study synthesizes the long-term shipborne observations and a LES model

490   to explore the phenomena of negative SAT-SST during advection fog over the NWP

491   (referred to ssH fog). The UCLA-LES successfully simulates a fog event with ssH fog

492   and captures the diurnal variation in SAT-SST during the fog episode. The simulation

493   results highlight the strong influence of the LWC effect at the fog top on the formation

494   of ssH fog.

495   Long-term shipborne observations reveal the prevalence of advection fog along

496   the cold flank of the SST front in the NWP during the boreal summer. The ssH fog often

497   occurs downstream of the regime of the advection fog with positive SAT-SST. The

498   relative frequency ssH during episodes of advection fog is ~27.5% in JJA, which is

499   roughly consistent with the results over the summertime Yellow Sea (Yang et al. 2021)

500   and wintertime northeast Pacific (Li et al. 2022). Furthermore, our findings reveal, for

501   the first time, that the relative frequency of ssH fog exhibits a distinct diurnal cycle,

502   with a peak occurrence (~34.5%) before sunrise and a trough occurrence (~18.8%) in

503   the afternoon (Fig. 2b). This suggests that the thermal dynamics and associated

504   turbulence structure of advection fog exhibit significant diurnal variation.

505   From a Lagrangian perspective, we utilize the turbulence-closure UCLA-LES

506   model to simulate an advection fog event over the NWP from 01 to 04 July 2013, which

507   exhibits similar characteristics to the observations of this sea fog case and long-term

508 features of ssH fog. Surprisingly, the LES model successfully reproduces the diurnal

509 variation in SAT-SST of the observations when incorporating diurnal solar radiation,

510 indicating that the model captures the essential processes responsible for ssH fog.

511 We analyzed the LES simulation with constant solar radiation in detail, which also

512 produces ssH fog during the advection fog episode. Before the fog formation, the

513 decreased SST over the oceanic front cools the near-surface air through the mechanical

514 turbulence and triggers fog occurrence. Around the fog initiation, the cold sea surface

515 drives a stable layer below 40 m in altitude, which decouples the fog layer from the sea

516 surface. Once the surface vapor condenses, in the perspective of the fog layer, the fog-

517 top LWC effect rapidly exceeds the near-surface mechanical cooling within ~2 hours

518 after the fog formation (Fig. 9), when the air column is still on the SST front. A thermal

519 turbulence interface, separating the layers characterized by thermal and mechanical

520 turbulence, well depicts the evolution of the vertical turbulence structure (Fig. 10a).

521 The thermal turbulence from the fog top gradually develops downward to transport the

522 fog-top LWC effect and reaches the surface 43 hours after the fog formation, leading to

523 the SAT drops below SST. The occurrence time of ssH fog and minimus SAT-SST (-

524 0.65 K) is close to observation result (-1 K).

525 In the LES simulation with diurnal cycle radiation, the enhancement of LWC

526 during night causes the thermal turbulent interface to reach the surface, leading to the

527 occurrence of ssH fog. At daytime, the thermal turbulent interface moves away from

528 the surface and SAT rises above SST due to weakened LWC. This result is consistent

529 with the observed variations in SAT-SST, while the simulated SAT-SST is weaker than

530 observations. This suggests that the LWC is underestimated in the model, which could

531 be related to the model vertical resolution.

532 Previous studies have primarily focused on the diurnal variation of fog frequency

533 using observational data and models (O'Brien et al. 2013; Liu et al. 2021), but there has

534 been a lack of research on the diurnal variation of air-sea temperature difference. The

535 reason is that sea fog evolution are not as strongly influenced by the diurnal variation

536 of surface temperature as radiation fog on land (Koračin and Dorman 2017), there is

537 weak variability in SST during sea fog episodes. Kim and Yum (2013) the investiged

the effect of diurnal variation in radiation on advection fog formation by PAFOG model but not discussed the diurnal variation in SAT-SST during fog due to the fog pireod is short. This paper verifies, from both observational and modeling perspectives, that sea fog exhibits significant diurnal variations in air-sea temperature difference, primarily regulated by LWC at the fog top and thermal turbulence.

Our LES results suggest ssH fog formation is characterized by a thermal turbulent layer, induced by the LWC at the fog top, that pervades the entire fog layer and cools the near-surface air below the sea surface temperature (SST). Previous studies primarily used on the near-surface liquid water in sea fog to validate the weather model performance in simulating sea fog (e.g., Gao et al. 2007; Yang et al. 2018; 2019). Considering the limited availability of observations on the vertical structure of fog over the open sea, the observations of air-sea temperature differences during advection fog events offers valuable insights for improving the modeling of the thermal turbulence induced by the LWC at the fog top. The presence of ssH fog signals a pronounced LWC at the fog top and thorough mixing of thermal turbulence within the layer. Consequently, refining weather models to account for air-sea temperature differences enables more precise sea fog simulations, espacially in terms of the thermal tubulence within fog layer. For instance, Yang et al. (2019) used top-down mixing parameterization in the WRF model to characterize turbulence from the fog top. While the thermal turbulence is explicitly resolved in UCLA-LES. Comparing these models' simulation results may refine the turbulence parameterization in weather models, a desirable aim for future research.

Yang et al. (2021) applied a weaker subsidence and did not simulated ssH fog. Our simulation results demonstrate that descending motion plays a important role in modulating the LWC at the fog top. Thus, stronger descending motion leads to longer fog duration (72 h vs 55 h in Yang et al. 2021) and lower fog top height (380 m vs 580 m in Yang et al. 202). These findings indicate that large-scale descending motion modulates the characteristics of fog by altering the fog-top LWC.

Acknowledgments. This work is supported by the National Key Research and

568 Development Program of China (2018YFA0605700), and the Natural Science

569 Foundation of China (41875012). L. Y. are supported by the National Key R&D

570 Program of China (2021YFB2601701), and S. D. are supported by Natural Science

571 Foundation of Shandong Province (ZR2019ZD12).

572

Open Research

Data Availability Statement

575 The data used in this study are obtained from the ECMWF which is available at

576 https://www.ecmwf.int/en/forecasts/datasets/reanalysis-datasets/era5 and the ICOADS

577 data at https://icoads.noaa.gov/.

578

579

Reference

Bari, D., Bergot, T., & Khlifi, M. E. (2016). Local meteorological and large scale weather characteristics of fog over the Grand Casablanca region, Morocco. *Journal of Applied Meteorology and Climatology*, 55(8), 1731–1745. https://doi.org/10.1175/JAMC-D-15-0314.1

Bergot, T. (2013). Small-scale structure of radiation fog: A large-eddy simulation study. *Journal of the Royal Meteorological Society*, 139, 1099–1112.

Bergot, T. (2016). Large-eddy simulation study of the dissipation of radiation fog. *Quarterly Journal of the Royal Meteorological Society*, 142, 1029–1040.

Bretherton, C. S., & Wyant, M. C. (1997). Moisture transport, lower-tropospheric stability, and decoupling of cloud-topped boundary layers. *Journal of the Atmospheric Sciences*, 54(1), 148–167. https://doi.org/10.1175/1520-0469(1997)054%3C0148:MTLTSA%3E2.0.CO;2

Douglas, C. (1930). Cold fogs over the sea. *Meteorological Magazine*, 65, 133–135.

Caldwell, P., Bretherton, C. S., & Wood, R. (2005). Mixed-layer budget analysis of the diurnal cycle of entrainment in southeast Pacific stratocumulus. *Journal of the Atmospheric Sciences*, 62(10), 3775-3791.

Curry, J.A., & Herman, G. F., (1985). Infrared radiative properties of summertime Arctic stratus clouds. *Journal of Climate Apply Meteoriligy*, 24, 525-538.

Draxler, R. R., & Rolph, G. D. (2010). HYSPLIT (HYbrid Single-Particle Lagrangian Integrated Trajectory) model access via NOAA ARL READY website (http://ready. arl. noaa. gov/HYSPLIT. php), NOAA Air Resources Laboratory. *Silver Spring*, MD, 25(1).

Findlater, J., Roach, W., & McHugh, B. (1989). The haar of north-east Scotland. *Quarterly Journal of the Royal Meteorological Society*, 115(487), 581–608.

Fu, Q., & Liou, K. N. (1993) Parameterization of the radiative properties of cirrus clouds. *Journal of the Atmospheric Sciences*, 50, 2008–2025.

Fu, G., & Song, Y. J. (2014). Climatic characteristics of sea fog frequency over the North Pacific Ocean. *Periodical of Ocean University of China*, 44(10), 35-41.

609   Gao, S., Lin, H., Shen, B., & Fu, G. (2007). A heavy sea fog event over the Yellow Sea
610   in March 2005: Analysis and numerical modeling. *Advances in Atmospheric*
611   *Sciences*, 24(1), 65–81. https://doi.org/10.1007/s00376-007-0065-2

612   Gerber, H., Malinowski, S. P., Brenguier, J. L., & Burnet, F. (2005). Holes and
613   entrainment in stratocumulus. *Journal of the Atmospheric Science*, 62, 443-459.

614   Gerber, H., Frick, G., Malinowski, S. P., Jonsson, H., Khelif, D., & Krueger, S. K.
615   (2013). Entrainment rates and microphysics in POST stratocumulus. *Journal of*
616   *Geophysical Research: Atmospheres*, 118, 1-16.

617   Gerber, H., Malinowski, S., Bucholtz, A. & Thorsen, T. (2014). Radiative Cooling of
618   Stratocumulus. Extended Abstract. 14 Atmospheric Radiation Conference,
619   American Meteorology Society, Boston, MA, 7-11 July, paper 9.3.

620   Guan, H., Yau, M. K., & Davies, R. (1997). The effects of longwave radiation in a small
621   cumulus cloud. *Journal of the Atmospheric Sciences*, 54(17), 2201–2214.
622   https://doi.org/10.1175/1520-0469(1997)054%3C2201:TEOLRI%3E2.0.CO;2

623   Gultepe, I., Tardif, R., Michaelides, S. C., Cermak, J., Bott, A., Bendix, J., et al. (2007).
624   Fog research: A review of past achievements and future perspectives. *Pure and*
625   *Applied Geophysics*, 164(6-7), 1121–1159. https://doi.org/10.1007/s00024-007-
626   0211-x

627   Hersbach, H., Bell, B., Berrisford, P., Hirahara, S., Horányi, A., Muñoz-Sabater, J., et
628   al. (2020). The ERA5 global reanalysis. *Quarterly Journal of the Royal*
629   *Meteorological Society*. https://doi.org/10.100

630   Hu, R. J., Dong, K. H., & Zhou, F. X. (2006). Numerical experiments with the advection,
631   turbulence and radiation effect in the sea fog formation process (in Chinese).
632   *Advance in Marine Science*, 24(2), 156–165.

633   Huang, H., Liu, H., Huang, J., Mao, W., & Bi, X. (2015). Atmospheric boundary layer
634   structure and turbulence during sea fog on the southern China coast. Monthly
635   Weather Review, 143(5), 1907-1923.

636   Schwenkel, J., & Maronga, B. (2019). Large-eddy simulation of radiation fog with
637   comprehensive two-moment bulk microphysics: Impact of different aerosol
638   activation and condensation parameterizations. *Atmospheric Chemistry and*

Physics, 19, 7165–7181.

Lamb, H. (1943). Haars or North Sea fogs on the coasts of Great Britain. Meteorology Office Publication M. O. 504, 24 pp.

Leipper, D. F. (1948). Fog development at San Diego, California. *Journal of Marine Research*, 7, 337–346.

Leipper, D. F. (1994). Fog on the U. S. West Coast, a review. *Bulletin of the American Meteorological Society*, 72, 229–240.

Lewis, J. M., Koračin, D., & Redmond, K. T. (2004). Sea fog research in the United Kingdom and United States: A historical essay including outlook. *Bulletin of the American Meteorological Society*, 85(3), 395–408.

Lilly, D. K. (1967). The representation of small scale turbulence in numerical simulation experiments. *IBM Scientific Computing Symposium on Environmental Sciences*, Yorktown Heights, NY, International Business Machines, 195–210.

Li, X., Zhang, S., Koračin, D., Yi, L., & Zhang, X. (2022). Atmospheric conditions conducive to marine fog over the northeast Pacific in winters of 1979–2019. *Frontiers in Earth Science*, 10, 942846.

Liu, J. W., Sun, Y., & Yang, L. (2021). Interannual variability in summertime sea fog over the Northern Yellow Sea and its association with the local sea surface temperature. *Journal of Geophysical Research: Atmospheres*, 126(15), e2020JD034439.

Long, J., Zhang, S., Chen, Y., Liu, J., & Han, G. (2016). Impact of the Pacific-Japan teleconnection pattern on July sea fog over the northwestern Pacific: Interannual variations and global warming effect. *Advances in Atmospheric Sciences*, 33, 511–521.

Jiang, H., Xue, H., Teller, A., Feingold, G., & Levin, Z. (2006). Aerosol effects on the lifetime of shallow cumulus. *Geophysical Research Letters*, 33, L1486.

Kim, C. K., & Yum, S. S. (2013). A study on the transition mechanism of a stratus cloud into a warm sea fog using a single column model PAFOG coupled with WRF. Asia-Pacific Journal of Atmospheric Sciences, 49, 245-257.

Kunkel, B. A. (1984). Parameterization of droplet terminal velocity and extinction

coefficient in fog models. *Journal of Climate Appllied Meteorology*, 23, 34–41, https://doi.org/10.1175/1520-0450(1984) 023,0034:PODTVA.2.0.CO;2.

Koračin, D., Leipper, D. F., & Lewis, J. M. (2005). Modeling sea fog on the U. S. California coast during a hot spell event. *Geofizika*, 22(1), 59–82.

Koračin, D., Lewis, J., Thompson, W. T., Dorman, C. E., & Businger, J. A. (2001). Transition of stratus into fog along the California coast: Observations and modeling. *Journal of the Atmospheric Sciences*, 58(13), 1714–1731. https://doi.org/10.1175/1520-0469(2001)058%3C1714:TOSIFA%3E2.0.CO;2

Koračin, D., & Dorman, C. E. (Eds.) (2017). *Marine fog: Challenges and advancements in observations, modeling, and forecasting* (pp., 291–343). Zurich: Springer International Publishing.

Maronga, B., & Reuder, J. (2017). On the formulation and universality of Monin-Obukhov similarity functions for mean gradients and standard deviations in the unstable surface layer: Results from surface-layer resolving large-eddy simulations. *Journal of the Atmospheric Sciences*, 74, 989 – 1010.

McGibbon, J., & Bretherton, C. S. (2017). Skill of ship-following large-eddy simulations in reproducing MAGIC observations across the northeast Pacific stratocumulus to cumulus transition region. *Journal of Advances in Modeling Earth Systems*, 9, 810–831.

Nakanishi, M. (2000). Large-eddy simulation of radiation fog. *Boundary-Layer Meteorolog*, 94, 461–493.

O'Brien, T. A., Sloan, L. C., Chuang, P. Y., Faloona, I. C., & Johnstone, J. A. (2013). Multidecadal simulation of coastal fog with a regional climate model. Climate Dynamics, 40, 2801–2812.

Petterssen, S. (1938). On the causes and the forecasting of the California fog. *Bulletin of the American Meteorological Society*, 19(2), 49–55.

Pincus, R., Baker, M. B., & Bretherton, C. S. (1997). What controls stratocumulus radiative properties? Lagrangian observations of cloud evolution. *Journal of the Atmospheric Sciences*, 54, 2215–2236.

Pincus, R., & Stevens, B. (2009). Monte Carlo spectral integration: A consistent

approximation for radiative transfer in large eddy simulations. *Journal of Advances in Modeling Earth Systems*, 1, 9.

Rodhe, B. (1962). The effect of turbulence on fog formation. *Tellus*, 14, 49-86.

Rogers, D. P., & Koračin, D. (1992). Radiative transfer and turbulence in the cloud-topped marine atmospheric boundary layer. *Journal of the Atmospheric Sciences*, 49(16), 1473–1486.

Savic-Jovcic, V., & Stevens, B. (2008). The structure and mesoscale organization of precipitating stratocumulus. *Journal of the Atmospheric Sciences*, 65, 1587–1605.

Seifert, A., & Beheng, K. D. (2001). A double-moment parameterization for simulating auto conversion, accretion, and self-collection. *Atmospheric Research*, 59–60, 265–281.

Smagorinsky, J. S. (1963). General circulation experiments with the primitive equations. Part I: The basic experiment. *Monthly Weather Review*, 91, 99–164.

Stevens, B. (2000). Cloud transition and decoupling in shear-free stratocumulus-topped boundary layers. *Geophysical Research Letters*, 27, 2557–2560.

Stevens, B., Stevens, B., Lenschow, D. H., Faloona, I., Moeng, C. H., Lilly, D. K., Blomquist, B., Vali, G., Bandy, A., Campos, T., Gerber, H., Haimov, S., Morley, B., & Thornton, D. (2003). On entrainment rates in nocturnal marine stratocumulus. *Quarterly Journal of the Royal Meteorological Society*, 129, 3469–3493.

Stevens, B., Moeng, C., Ackerman, A. S., Bretherton, C. S., Chlond, A., de Roode, S., Edwards, J., Golaz, J., Jiang, H., Khairoutdinov, M., Kirkpatrick, M. P., Lewellen, D. C., Lock, A., Müller, F., Stevens, D. E., Whelan, E., & Zhu, P. (2005). Evaluation of large-eddy simulations via observations of nocturnal marine stratocumulus. *Monthly Weather Review*, 133, 1443–1462.

Stevens, B. (2010). Introduction to UCLA-LES: Version 3.2. 1. MPI Doc., 20 pp.

Taylor, G. I. (1917). The formation of fog and mist. *Quarterly Journal of Royal Meteorological Society*, 43(183), 241–268. https://doi.org/ 10.1002/qj.49704318302

Tokinaga, H., & Xie, S. P. (2009). Ocean tidal cooling effect on summer sea fog over

the Okhotsk Sea. *Journal of Geophysical Research: Atmospheres*, 114, D14102.

Trémant, M. (1987). La prévision du brouillard en mer. Météorologie Maritimeet Activities. Oceanograpiques Connexes Raport, WMO, 20, 127.

Wang, B. H. (1985). *Sea fog* (p., 2). Beijing: China Ocean Press.

Wainwright, C., & Richter, D. (2021). Investigating the sensitivity of marine fog to physical and microphysical processes using large-eddy simulation. *Boundary-Layer Meteorology*, 181, 473-498.

Wyant, M. C., Bretherton, C. S., Rand, H. A., & Stevens, D. E. (1997). Numerical simulations and a conceptual model of the stratocumulus to trade cumulus transition. *Journal of the Atmospheric Sciences*, 54, 168–192.

Yamaguchi, T., & Randall, D. A. (2008). Large-eddy simulation of evaporatively driven entrainment in cloud-topped mixed layers. *Journal of the Atmospheric Sciences*, 65(5), 1481–1504.

Yang, Y., Hu, X. M., Gao, S., & Wang, Y. (2018). Sensitivity of WRF simulations with the YSU PBL scheme to the lowest model level height for a sea fog event over the Yellow Sea. *Atmospheric Research*, 215, 253–267.

Yang, Y., & Gao, S. (2019). The impact of turbulent diffusion driven by fog‐top cooling on sea fog development. Journal of Geophysical Research: Atmospheres, 125, e2019JD031562. https://doi.org/10.1029/2019JD031562

Yang, L., Liu, J. W., Ren, Z. P., Xie, S. P., Zhang, S. P., & Gao, S. H. (2018). Atmospheric conditions for advection-radiation fog over the Western Yellow Sea. *Journal of Geophysical Research: Atmospheres*, 123, 5455–5468. https://doi.org/10.1029/2017JD028088

Yang, L., Liu, J. W., Xie, S. P., & Shen, S. S. (2021). Transition from fog to stratus over the northwest Pacific Ocean: Large-eddy simulation. *Monthly Weather Review*, 149, 2913-1925.

Zhang, S. P., & Ren, Z. P. (2010). The influence of thermal effects of underlaying surface on the spring sea fog over the Yellow Sea—Observations and numerical simulation (in Chinese). *Acta Meteorologica Sinica*, 68, 116–125.

758   Zhang, S. P., Li, M., Meng, X. G., Fu, G., Ren, Z. P., & Gao, S. H. (2012). A comparison

759   study between spring and summer fogs in the Yellow Sea—Observations and

760   mechanisms. *Pure and Applied Geophysics*, 169(5-6), 1001–1017.

761   https://doi.org/10.1007/s00024-011-0358-3

762   Zhang, S., Chen, Y., Long, J., & Han G. (2014). Interannual variability of sea fog

763   frequency in the Northwestern Pacific in July. *Atmospheric Research*, 151, 189–

764   199.

765